

# Structural, mechanical, electronic, thermal, and optical properties of the inverse-Heusler compounds $X_2RuPb(X = La, Sc)$ : A first-principles investigation

A. Bouazza<sup>a,\*</sup>, M. Khirat<sup>b</sup>, M. Larbi<sup>c</sup>, N. Bettahar, and D. Rached

<sup>a</sup>*L2GEGI Laboratory, University of Tiaret, 14000 Tiaret, Algeria.*

*\*e-mail: abdelkader.bouazza@univ-tiaret.dz*

<sup>b</sup>*Magnetic Materials Laboratory Djillali Liabes University of Sidi Bel-Abbes, 22000 Sidi Bel-Abbes, Algeria.*

<sup>c</sup>*Physics Department, Djillali Liabes University of Sidi Bel-Abbes, 22000 Sidi Bel-Abbes, Algeria.*

Received 8 September 2022; accepted 25 March 2023

Topological insulators are novel quantum material states with insulating bulk band gaps and topologically protected metallic surface states that have been extensively studied owing to their intriguing properties for spintronic and quantum-computing applications. The structural, mechanical, electronic, thermal, and optical properties of inverse Heusler compounds  $La_2RuPb$  and  $Sc_2RuPb$  in two  $Hg_2CuTi$ ,  $Cu_2MnAl$ -type structures were calculated using the full potential linear muffin-tin orbital simulation methodology as implemented in the computer code, which is based on density functional theory. We employed the local-density approximation for the exchange and correlation potential (XC) terms. Consequently, the optical characteristics of  $La_2RuPb$ ,  $Sc_2RuPb$  and elastic constants  $C_{ij}$  and their corresponding elastic moduli were computed for the first time. According to our structural calculations,  $La_2RuPb$  is more stable in its  $Hg_2CuTi$ -type structure than  $Sc_2RuPb$  in its  $Cu_2MnAl$ -type structure. However, the mechanical characteristics demonstrate their stability in the final stages of elastic deformation.

**Keywords:** Inverse-Heusler compounds; density functional theory; topological insulators; mechanical properties; optical properties; elastic constants.

DOI: <https://doi.org/10.31349/RevMexFis.69.050501>

## 1. Introduction

Since Heusler compounds are likely to be fresh prospects for future uses, they have rekindled the attention of researchers. Intermetallic Heusler compounds are ternary ferromagnetic compounds with the general formula  $X_2YZ$ , which were initially identified in 1903 by German mining engineer Friedrich Heusler while examining the  $Cu_2MnSb$  alloy [1, 2].

Based on their estimated electronic band structures, a novel class of Heusler alloys was anticipated to be labeled “multifunctional topological insulation (TIs)”. Surface states are topologically safeguarded against impurity fusion in this new state of matter [3, 4].

Because of their diverse properties for spintronic applications [5, 6], optoelectronics [7], superconductivity [8], shape-memory [9], giant magnetoresistance spin-valve (GMR) [10], thermoelectric applications [11], and spin injection to semiconductors [12], interest in them is steadily growing as in the thin film deposition technology [13–15].

Several theoretical and experimental attempts have been made to anticipate novel topological insulators (TIs) due to their enormous promise in spintronics and quantum computing [16, 17]. (TIs) are a relatively novel material class. Their narrative begins with Bernevig and König’s [18, 19] initial prediction of (HgTe) as a material (TI). Following this finding, (TIs) materials in binary compounds of (II-VI) group elements have been thoroughly explored.

Full-Heusler alloys are ternary intermetallic compounds with the stoichiometric composition  $X_2YZ$  [1, 20], where  $X$

and  $Y$  are transition metal elements and  $Z$  is a (III-, IV-, or V-group element). These materials have a cubic crystal shape. Full-Heusler compounds have been found in either  $Hg_2CuTi$ -form, designated X-form  $F\bar{4}3m$  symmetry (space group  $N^\circ 216$ ) [21], or the  $(Cu_2MnAl)$ -form denoted as the  $L_{21}$ -type). When the (X) component’s valence electron number is greater than the (Y) ones, the compound adopts the  $L_{21}$ -type structure [20, 21], but the X-type structure is preferred in the opposite situation [22]. The unit cell of the  $L_{21}$ -type shape belonging to the  $Fm\bar{3}m$  symmetry (space group  $N^\circ 225$ ) [12, 23] is made up of four interpenetrating (FCC) (Face Centered Cubic sublattices) with the following Wyckoff coordinates:  $X_1 = (0, 0, 0)$ ,  $X_2 = (1/2, 1/2, 1/2)$ ,  $Y = (1/4, 1/4, 1/4)$ ,  $Z = (3/4, 3/4, 3/4)$ . The occupancy parameters of the X2 and Y components are swapped in the (X-type) structure. Inverse Heusler compounds are complete Heusler compounds with a later prototype architecture.

If the two X particles seem no longer equivalent, ternary and quaternary Full-Heusler alloys are formed. Quaternary Heusler alloys with a stoichiometric composition of  $(XX'YZ)$  commonly crystallize as the group  $N^\circ 216$  [24–26]. The following Wyckoff coordinates  $X = (1/2, 1/2, 1/2)$ ,  $X' = (0, 0, 0)$ ,  $Y = (1/4, 1/4, 1/4)$ ,  $Z = (3/4, 3/4, 3/4)$  are occupied in the unit cell for the (Y-type) structure. The search for (TIs) has recently expanded to include ternary Heusler and chalcopyrite compounds [3, 27]. Zhang et al. revealed that most inverse Heusler compounds show an inverted band order, a promising characteristic of topological insulators. However, their topological insulating state is re-

ported to be sensitive to uniaxial strain and variations in the lattice constants [28].

Understanding a material's physical qualities is essential for understanding its features in terms of its operational uses [29–32]. To better understand the behavior of the  $\text{La}_2\text{RuPb}$ ,  $\text{Sc}_2\text{RuPb}$  compounds, we present our calculations on the structural, mechanical, electrical, and optical characteristics of the compounds in their phases  $\text{Hg}_2\text{CuTi}_2$ ,  $\text{Cu}_2\text{MnAl}$ -Type, respectively.

These analyses are used to calculate the phase transitions and other essential ground state features of these structures. In addition, electronic band structures are also established to comprehend the properties of the (TIs). Our calculations were carried out in the context of density functional theory (DFT) utilizing the local density approximation (LDA), employing the full-potential linear muffin-tin orbital (FPLMTO) approach as implemented in the computer code (LmtART).

To our knowledge, no theoretical or practical study on the electronic states and characteristics of these Heusler alloys has been conducted.

The following is how the remainder of the paper is organized: Section 2 contains computational details and the calculation technique, Sec. 3 has the findings of the structural, mechanical, electronic, and optical characteristics, as well as discussion, and Sec. 4 concludes with a short conclusion.

## 2. Computational details

Several approaches may be used to determine the physical characteristics of materials, such as electronic structures. The technique of augmented plane waves (FP-LAPW) [33, 34] and the full-potential linear muffin-tin orbital (FP-LMTO) [35, 36] are two of the most well-known ab-initio approaches that are applicable. Moreover, it may be used to solve the (DFT) equations [37], the most widely used and effective method for many years. It also has the benefit of addressing numerous atoms. The latter is now in the tens of thousands and might rise to the hundreds of thousands in the coming years. The calculations given here were performed using the Perdew-Wang (P.W) [38] model and the (FP-LMTO) technique built inside the (DFT) as incorporated in the (LmtART MStudio MindLab 5-code) produced by S.Y Savrasov [39].

A portion of the overall energy calculations for the potential of exchange and correlation (XC) (energy/potential) was done using the local density approximation (LDA) [40]. Compared to prior versions of the (LMTO) approach, this

version of (FP-LMTO) incorporates significant enhancements. The charge density/crystal potential is not subjected to any shape approximation. Furthermore, in this computational strategy, known as (FP-LMTO), the crystal unit cell is partitioned into the muffin-tin (MT) sphere region and the interstitial region (IR) for mathematical convenience, and both zones are handled on the same footing, increasing the accuracy of the eigenvalue results. Furthermore, a complete foundation is employed in this technique. For the spherical component of the potential, fundamental functions are defined in numerical solutions of the radial Schrödinger equation multiplied by spherical harmonics, while basis functions are given in terms of Fourier series for the (IR) regions. Charge density and the related potential were presented within the ( $MT$ ) spheres, up to ( $l_{\max} = 6$ ), using spherical harmonics to carry out calculations for the ( $\text{La}_2\text{RuPb}$ ) and ( $\text{Sc}_2\text{RuPb}$ ) compounds. The k-points integration was carried out using the tetrahedron method [41] over the irreducible edge of the first Brillouin region using a (K-point) grid of (10, 10, 10). At the same time, the criterion of convergence up to ( $10^{-5}$ ) was met self-consistently for the accurate calculations of total energy and charge density.

## 3. Results and discussion

### 3.1. Phase transition and structural properties

In this part, we estimated the structural characteristics of the two full Heusler alloys  $\text{La}_2\text{RuPb}$ ,  $\text{Sc}_2\text{RuPb}$  and looked at both structural phases  $\text{Hg}_2\text{CuTi}$ ,  $\text{Cu}_2\text{MnAl}$  by utilizing the total energy minimization approach (at  $T = 0^\circ\text{K}$ ) for the determination of the equilibrium lattice constant. Calculating the total energy as a volume function was used to optimize the unit cell volume  $V$ . Finally, the change of total energy  $E_{\text{TOT}}$  with volume  $V$  is fitted using Murnaghan's equation of state [42, 43] to yield the equilibrium lattice constant and the bulk modulus:

$$E(V) = E_0 + \frac{B_0 V}{B'} \left[ \left( \frac{V}{V_0} \right)^{B'} \frac{1}{B' - 1} + 1 \right] - \frac{B_0 V_0}{B' - 1}, \quad (1)$$

where  $E_0$  is the ground-state total energy,  $V_0$  is the optimal unit-cell volume, and  $B_0$  and  $B'$  are the bulk modulus and its pressure derivative.

Table II lists our results and additional information for the optimized lattice constants for both compounds.

Since we are not aware of any experimental data, we compare our results with those obtained in the already-published papers of Y. Lakred and co-workers [28], A. Bahlouli and co-workers [29] for the inverse-Heusler alloys  $X_2\text{RuPb}$ , and X.M. Zhang and co-authors [30] for the  $Y_2\text{RuPb}$  investigations. Our computed values are in good correlation and agreement with those obtained by the researchers mentioned above (see Table II), which confirm the precision of our obtained results.

TABLE I. RMT (a.u.) of Ru, Pb, and X atoms for  $X_2\text{RuPb}$  compounds.

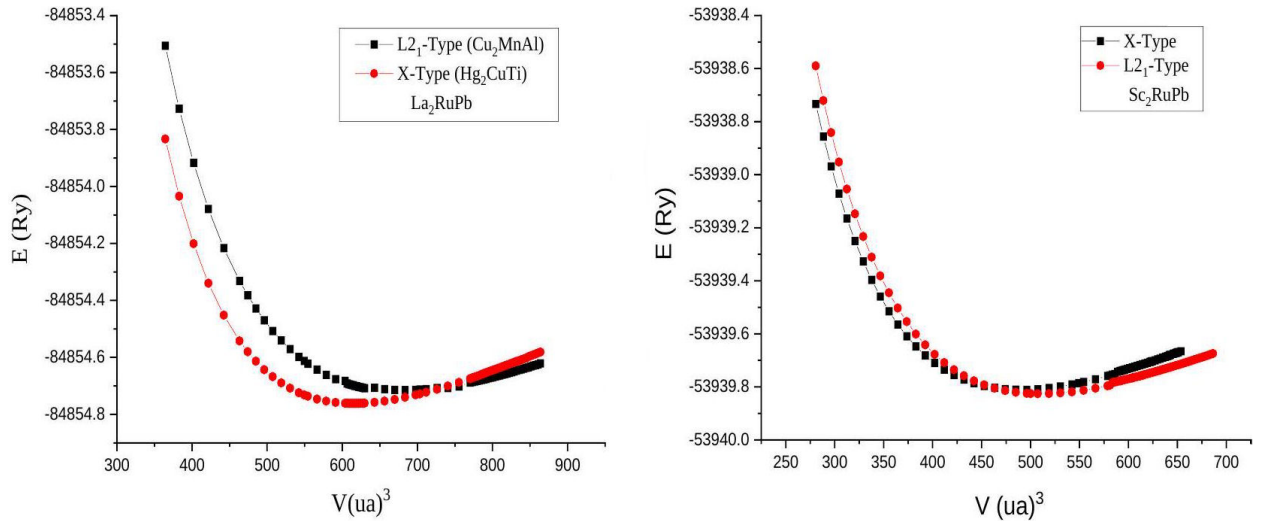
Atom	$\text{La}_2\text{RuPb}$	$\text{Sc}_2\text{RuPb}$
X	2.929	2.696
Ru	2.901	2.807
Pb	2.956	2.807

TABLE II. Equilibrium lattice constants  $a_0$  ( $\text{\AA}$ ) and total energy  $E$  (Ry/unit cell) for (La RuPb, Sc<sub>2</sub>RuPb) compounds.

Compound	Calculation	$a_0$ ( $\text{\AA}$ )	Energy E (Ry/unit cell)
La <sub>2</sub> RuPb		7.3760 [28]	-84911.718
	Other (Theory)	7.3417 [29]	-84911.720
		7.3470 [30]	-
	Our calculation	7.1597 [LDA] X- Type	-84854.71837
		7.5746 [GGA] L2 - Type	-84854.7606
		7.3962 [LDA] L2 2 <sub>1</sub> - Type	-84911.68004
7,338 [GGA] X - Type		-84911.6587	
Experimental	-	-	
Sc <sub>2</sub> RuPb		6.7460 [28]	-53978.04810
	Other (Theory)	6.7531 [29]	-53978.02600
		6.6705 [30]	-
	Our calculation	6.6342 [LDA] X- Type	-53939.81095
		6.7263 [LDA] L2 2 <sub>1</sub> - Type	-53939.82301
		6.7934 [GGA] X - Type	-53978.00554
6.7237 [GGA] L2 2 <sub>1</sub> - Type		-53939.82461	
Experimental	-	-	

TABLE III. The calculated equilibrium lattice parameter  $a_0$  ( $\text{\AA}$ ), primitive-cell volume  $V_0$  ( $\text{\AA}^3$ ), bulk modulus  $B_0$  GPa, its pressure derivative  $B'$  and the equilibrium energy  $E_0$  Ryd for the La<sub>2</sub>RuPb, Sc<sub>2</sub>RuPb compound in the Hg<sub>2</sub>CuTi, Cu<sub>2</sub>MnAl-type structures.

System	structure-type	$a$	$V_0$	$B_0$	$B'$	$E_0$
L a <sub>2</sub> RuPb	Hg <sub>2</sub> CuTi	7.1597	91.7538	93.4167	4.72155	-84854.7606
Sc <sub>2</sub> RuPb	Cu <sub>2</sub> MnAl	6.7263	76.0796	127.6952	4.05872	-53939.82301

FIGURE 1. The variation of the total energy as a function of the volume for the compounds La<sub>2</sub>RuPb, Sc<sub>2</sub>RuPb in the Hg<sub>2</sub>CuTi, Cu<sub>2</sub>MnAl-type structures respectively.

The theoretical values supplied in the table using the (GGA) approximation match with our estimated lattice constants for La<sub>2</sub>RuPb, Sc<sub>2</sub>RuPb. Unfortunately, to our knowledge, no experimental data for these compounds have been published.

The variation of total energy as a function of volume for the La<sub>2</sub>RuPb, Sc<sub>2</sub>RuPb compounds in the Hg<sub>2</sub>CuTi, Cu<sub>2</sub>MnAl-type structures are shown in Fig. 1. Table III shows the obtained values for the  $a = \sqrt[3]{4V_0}$ ,  $E_0$ ,  $V_0$ ,  $B'$  and  $B_0$  parameters. To the best of our knowl-

edge, there is no data in the scientific literature that can be compared to the findings we've achieved.

As shown in Fig. 1, the  $\text{Hg}_2\text{CuTi}$ -type structure is found to be the most stable phase for the  $\text{La}_2\text{RuPb}$  compound at zero pressure because the crossing of the  $E(V)$  curve of the  $\text{Hg}_2\text{CuTi}$ -phase is before the curve of the  $\text{Cu}_2\text{MnAl}$ -phase for the lowest energy values, while the  $\text{Sc}_2\text{RuPb}$  compound is favored in the reverse case  $\text{Cu}_2\text{MnAl}$ -phase.

We believe that the values we discovered and described in the table above are consistent with those that will be found in the future by others when studying the two compounds in this or other ways, even though there was no theory or experimental values to compare them with our knowledge. The calculations of the structural properties of the two structures phases are reliable. These values encourage future experimental work to collaborate with our calculated results.

### 3.2. Elastic properties

The study of the mechanical properties of materials is significant for practical applications. The elastic properties of a solid are determined by the abovementioned elastic constants, which link the mechanical and dynamic behavior of a crystal and provide crucial information about the nature of the forces acting on the solid. The elastic constants, in particular, are macroscopic quantities that describe the stability, stiffness, and anisotropy of materials in inhomogeneous solids.

Understanding interatomic interactions are possible because of the influence of hydrostatic pressure. Mechanical stability and phase transition mechanisms stress to deformations allow for the evaluation of the wave's elastic straps' speed of propagation, as well as the assessment of mechanical properties such as ductility/brittleness, specific heat, hardness, melting point, Debye temperature, and thermal expansion coefficient [44]. Furthermore, elastic constants may be used to calculate the bulk modulus, shear modulus, Young's modulus, and Poisson's ratio, which are all important in calculating the strength of materials [45].

By studying the impact of hydrostatic pressure, we may learn about interatomic interactions, phase transition, and mechanical stability processes. Stresses to deformations may be used to measure mechanical qualities such as ductility/brittleness, specific heat, hardness, melting point, Debye temperature, and thermal expansion coefficient, as well as the speed of propagation of the wave's elastic straps [44]. Furthermore, elastic constants may be used to calculate the bulk modulus, shear modulus, Young's modulus, and Poisson's ratio, which are all critical in calculating the strength of materials [45].

Using stress-strain equations, the second-order elastic constants ( $C_{ij}$ ) for the  $\text{La}_2\text{RuPb}$ ,  $\text{Sc}_2\text{RuPb}$  compounds in the  $\text{Hg}_2\text{CuTi}$ ,  $\text{Cu}_2\text{MnAl}$ -type respectively, structure were calculated in this work. Total energy calculations are performed with regard to volume conserving stresses using the Mehl approach [46] as described in Ref. [47] to obtain the

( $C_{ij}$ ) values. Only three elastic constants ( $C_{11}$ ,  $C_{12}$ ) and ( $C_{44}$ ) are required to demonstrate the mechanical behavior of a cubic crystal and to satisfy the Born Huang criteria for positive assuredness of the stiffness matrix [48]. ( $C_{44} > 0$ ,  $C_{11} > C_{12}$ ), ( $(C_{11} + 2C_{12}) > 0$ ) are wellknown requirements for cubic crystal mechanical stability [49]. We utilized the averaged values of the Voigt approximation (the Voigt shear modulus  $G_v$ ) [50] and the Reuss approximation (the Reuss shear modulus  $G_r$ ) [51] to derive the bulk structural parameters.

For investigation of the material hardness, the elastic properties, *e.g.*, bulk modulus  $B$ , Voigt-Reuss-Hill shear modulus  $G_{VRH}$  [52] and the elastic Zener anisotropy factor  $A$  [53] are given by the following formulas for cubic crystal:

$$B_v = B_r = \frac{C_{11} + 2C_{12}}{3}, \quad (2)$$

$$B = \frac{B_r + B_v}{2}, \quad (3)$$

$$G_v = \frac{C_{11} - C_{12} + 3C_{44}}{5}, \quad (4)$$

$$G_r = \frac{5(C_{11} - C_{12})C_{44}}{3(C_{11} - C_{12}) + 4C_{44}}, \quad (5)$$

$$G_{VRH} = \frac{G_r + G_v}{2}, \quad (6)$$

$$E = \frac{9BG}{3B + G}, \quad (7)$$

$$v = \frac{3B - 2G}{2(3B + G)}, \quad (8)$$

$$A = \frac{2C_{44}}{C_{11} - C_{12}}. \quad (9)$$

Table IV shows the set of values that were obtained using the local density approximation (LDA) for the elastic constants and elastic moduli ( $C_{11}$ ,  $C_{12}$ ,  $C_{44}$ ), Young modulus  $E$ , shear modulus  $G$ , Poisson's ratio  $v$  and Anisotropy parameter  $A$ , the  $B/G$  ratio.

It is worth noting that each elastic constant meets the conditions listed above in the case of the compounds of concern  $\text{La}_2\text{RuPb}$ ,  $\text{Sc}_2\text{RuPb}$ . Bulk modulus also meets the requirement ( $C_{12} < B < C_{11}$ ) [54], indicating that both compounds are mechanically stable at ambient conditions with elastic deformation in the two  $\text{Hg}_2\text{CuTi}$ ,  $\text{Cu}_2\text{MnAl}$ -type structures.

The Poisson's ratio plays a significant role in distinguishing between covalent and Mod ionic materials, as a small value of Poisson's ratio of around  $v = 0.1$  characterizes covalent materials and around  $v = 0.25$  characterizes ionic materials [55, 56]. In this study, note that the determined Poisson's ratio values  $v$  in both types of structures of the two compounds are more significant than the critical value 0.25 of the ionic materials, indicating that these materials are ionic.

Furthermore, we refer to Frantsevich and co-authors [55], who differentiate the ductility and brittleness of materials by the  $B/G$  ratio to comprehend the ductile and brittle

nature of any compound. Frantsevich [57] further links the (ductility/brittleness) behavior to the Poisson's ratio value  $\nu$ , which is smaller than 0.33 for brittle materials and more than 0.33 for ductile materials.

The calculated value of the Poisson's ratio  $\nu$ , for  $\text{La}_2\text{RuPb}$  is less than (0.33), classifying this compound as brittle in the  $\text{Hg}_2\text{CuTi}$ -type structure, whereas  $\nu$  for  $\text{Sc}_2\text{RuPb}$  is more than 0.33, qualifying this compound as ductile in the  $\text{Cu}_2\text{MnAl}$ -type structure.

The critical value for distinguishing ductile and brittle materials is 2.76 for the  $B/G$  ratio. If the  $B/G$  ratio is greater than 2.76, the material behaves in a ductile manner. Otherwise, the material behaves in a brittle manner.

In the  $\text{Hg}_2\text{CuTi}$ ,  $\text{Cu}_2\text{MnAl}$ -type structure, the calculated values of  $B/G$  ratio are (2.4048, 2.6879) for both compounds  $\text{La}_2\text{RuPb}$ ,  $\text{Sc}_2\text{RuPb}$ , respectively, where these values are less than the critical value of 2.76, demonstrating the brittle nature of both these materials in this type structures.

However, these compounds may be categorized as ductile materials using Pugh's criteria ( $B/G$ ) ratio [58], which distinguishes ductility from brittleness for materials with a value of 1.75.

These findings are still theoretical research, which we intend to contradict shortly with experimental experiments.

We must know the value of the shear anisotropic factor  $A$  to comprehend the elastic anisotropic degree possessed by that composite. The elastic anisotropy  $A$  has a significant meaning in industrial science as it identifies micro-fractures in materials.

TABLE IV. The calculated single crystal elastic constants  $C_{ij}$ , and the polycrystalline elastic modulus: [shear modulus  $G$ , Voigt shear modulus  $G_v$ , Reuss shear modulus  $G_r$ , Young's modulus  $E$ , the Lamé's first parameter  $\lambda$  in GPA, Poisson's ratio  $\nu$ ,  $B/G$  ratio and the shear anisotropic factor  $A$  for the  $\text{La}_2\text{RuPb}$ ,  $\text{Sc}_2\text{RuPb}$  compounds in the  $\text{Hg}_2\text{CuTi}$ ,  $\text{Cu}_2\text{MnAl}$ -type structures.

Parameter	$\text{La}_2\text{RuPb}$ in the $\text{Hg}_2\text{CuTi}$ -type structure	$\text{Sc}_2\text{RuPb}$ in the $\text{Cu}_2\text{MnAl}$ -type structure
$C_{11}$	117.4	159.3
$C_{12}$	88.8	121.5
$C_{12}$	79.8	93.3
$G$	40.888	49.889
$E$	107.732	133.155
$\nu$	0.3174	0.3345
$A$	5.58	4.9365
$B_r$	98.333	134.1
$B_v$	98.333	134.1
$G_r$	28.17	36.238
$G_v$	53.6	63.54
$\lambda$	71.074	100.84
$B/G$	2.4048	2.6879

Where:

1. The composite is termed isotropic if the value of  $A = 1$  [59,60].
2. The composite is deemed anisotropic if it deviates from the unit value for  $A$  (High / Low  $A < 1$  or  $A > 1$ ).

So, for  $\text{La}_2\text{RuPb}$ ,  $\text{Sc}_2\text{RuPb}$  composites in the two phases'  $\text{Hg}_2\text{CuTi}$ ,  $\text{Cu}_2\text{MnAl}$  respectively, the values in Table IV above for the factor shear anisotropic  $A$  and computed by the (LDA) approximation, show anisotropic behavior and have a low probability of developing micro-cracks or structural defects during their growing process.

### 3.3. Thermal properties (Debye temperature, Sound velocity)

The thermal characteristics dictate the best circumstances for crystal formation to begin and sustain quality. We calculate the Debye temperature  $\theta_D$ , an essential basic parameter for a solid's thermodynamic characteristics, and it is linked to numerous physical properties such as specific heat, melting temperature, and elastic stiffness constants [61].

It may also distinguish between high and low-temperature areas in solids, with a greater  $\theta_D$  indicating higher thermal conductivity and melting temperature. It is found in equations describing properties arising from atomic vibrations and phonon theories; the determination of  $\theta_D$  using elastic constants at low temperatures will be the same as that of specific heat measurements, and the vibrational excitations at low temperatures are due to acoustic modes, *i.e.*, when  $\theta_D$  is connected with lattice vibrations.

Because  $\theta_D$  is proportional to the average sound velocity  $v_m$ , one of the traditional techniques of determining the Debye temperature is by using constant elastic data [60,61]. As a result, the following classical equation [62,63] may be used to estimate it:

$$\theta_D = \left( \frac{h}{k_B} \right) \left| \frac{3n}{4\pi} \left( \frac{N_A \rho}{M} \right) \right|^{\frac{1}{3}} v_m, \quad (10)$$

where  $h$  is Planck's constant,  $k_B$  is Boltzmann's constant,  $N_A$  is Avogadro's number,  $\rho$  is the density,  $M$  is the molar mass and  $n$  is the number of atoms in the unit cell.

From specific heat measurements the  $\theta_D$  can be calculated by the following relation [64]:

$$\theta_D = \left( \frac{200}{V^{1/3}} \right) \left( \sqrt{\frac{T_m}{M}} \right), \quad (11)$$

where  $V$  the molar volume in  $\text{cm}^3/\text{mol}$ ,  $M$  is the molar mass in  $\text{g/mol}$ , and  $T_m$  the melting point in Kelvin  $^\circ\text{K}$ .

For the polycrystalline material, the average sound velocity  $v_m$  can be calculated by the following relation [62,65]:

$$v_m = \left[ \frac{1}{3} \left( \frac{2}{v_t^3} + \frac{1}{v_l^3} \right) \right]^{-\left(\frac{1}{3}\right)}, \quad (12)$$

TABLE V. The calculated longitudinal, transverse, and average sound velocity  $v_l, v_t$ , and  $v_m$ , in  $\text{ms}^{-1}$  and the Debye temperature  $\theta_D$ , in  $^\circ\text{K}$  for the  $\text{La}_2\text{RuPb}$ ,  $\text{Sc}_2\text{RuPb}$  compounds in the  $\text{Hg}_2\text{CuTi}$ ,  $\text{Cu}_2\text{MnAl}$ -type structures.

Compound	Type-structure	$v_t$	$v_l$	$v_m$	$(\theta_D)$
$\text{La}_2\text{RuPb}$	$\text{Hg}_2\text{CuTi}$	1503.126	2906.234	1682.709	209.226
$\text{Sc}_2\text{RuPb}$	$\text{Cu}_2\text{MnAl}$	1780.955	3571.375	1998.211	269.598

where  $v_t$  and  $v_l$  represent the transverse and longitudinal sound velocities, which are obtained by using the shear modulus  $G$ , the bulk modulus  $B$  and the density  $\rho$  by employing the Navier's equation as found in Refs. [67, 68] and is given below:

$$v_l = \sqrt{\frac{3B + 4G}{3\rho}}, \quad (13)$$

$$v_t = \sqrt{\frac{G}{\rho}}. \quad (14)$$

Table V shows the calculated results of the  $(v_t, v_l, v_m)$ , and the  $\theta_D$  for the present compounds  $\text{La}_2\text{RuPb}$ ,  $\text{Sc}_2\text{RuPb}$  in the  $\text{Hg}_2\text{CuTi}$ ,  $\text{Cu}_2\text{MnAl}$  phases.

There has never been a complete investigation of the characteristics of these essential chemicals in the literature before. Consequently, our current findings may anticipate future trials and other theoretical investigations, revealing its true potential for appropriate applications under various situations.

One can clearly observe from this table that the  $\theta_D$  of the studied compounds are found to be in the following order  $\text{La}_2\text{RuPb} < \text{Sc}_2\text{RuPb}$  in the  $\text{Hg}_2\text{CuTi}$ ,  $\text{Cu}_2\text{MnAl}$ -type structure respectively. This behavior is related to the atomic

bonding of these materials, and this is due to the difference observed in the atomic number  $Z$  of the (Sc, La) atoms, where the (La) has a large number  $Z = 57$  of electrons, whereas the Sc has a small number  $Z = 21$ , leading to a radius increase and thus a decrease in temperature.

### 3.4. Electronic and optical properties

#### 3.4.1. Electronic properties

The study of electronic properties is crucial because it allows us to investigate and comprehend the nature of the bonds between the material's atoms.

In addition, the state density (DOS) is a necessary physical quantity for identifying a material's physical characteristics. It may offer access to a material's electronic and transport characteristics and an estimate of the number of binding and anti-binder states in the population with a particular energy. It also gives us access to data on electronic conductivity. Furthermore, for each atom, the electronic density is projected onto spherical harmonics of types p, d, or f, inside a sphere of a specified radius. As a result, partial state densities are produced, allowing the chemical bonding between

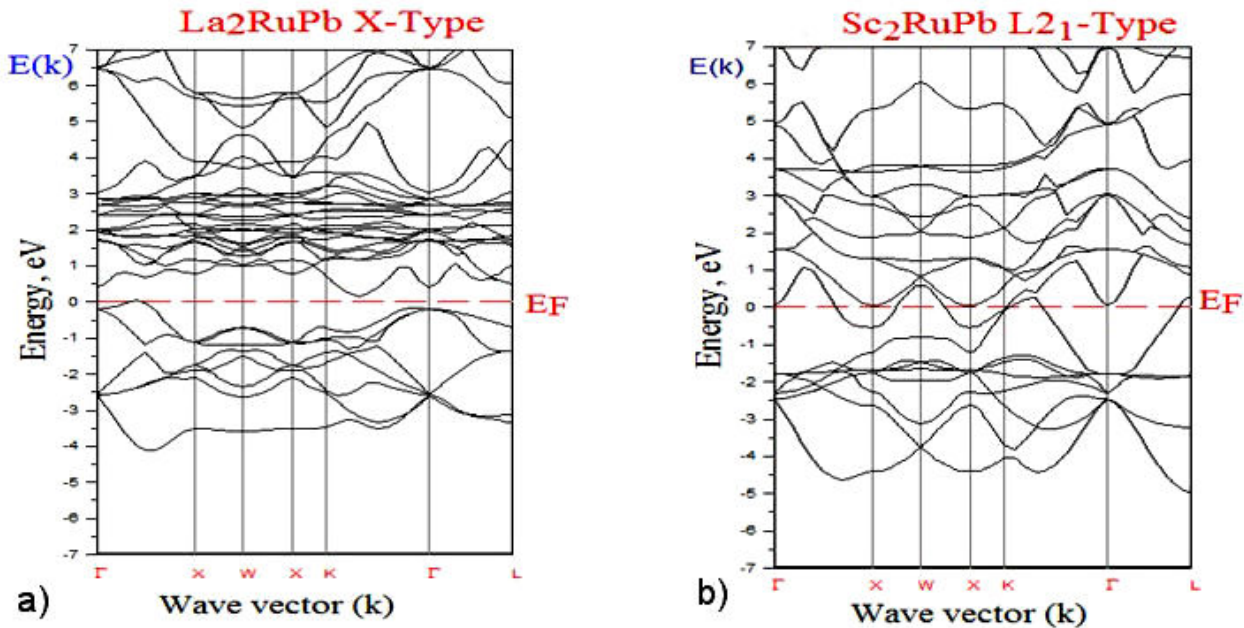


FIGURE 2. The bands structures along the symmetry lines of the Brillouin zone at the equilibrium lattice constant for the a)  $\text{La}_2\text{RuPb}$  and b)  $\text{Sc}_2\text{RuPb}$  compounds in the  $\text{Hg}_2\text{CuTi}$ ,  $\text{Cu}_2\text{MnAl}$ -type structures.

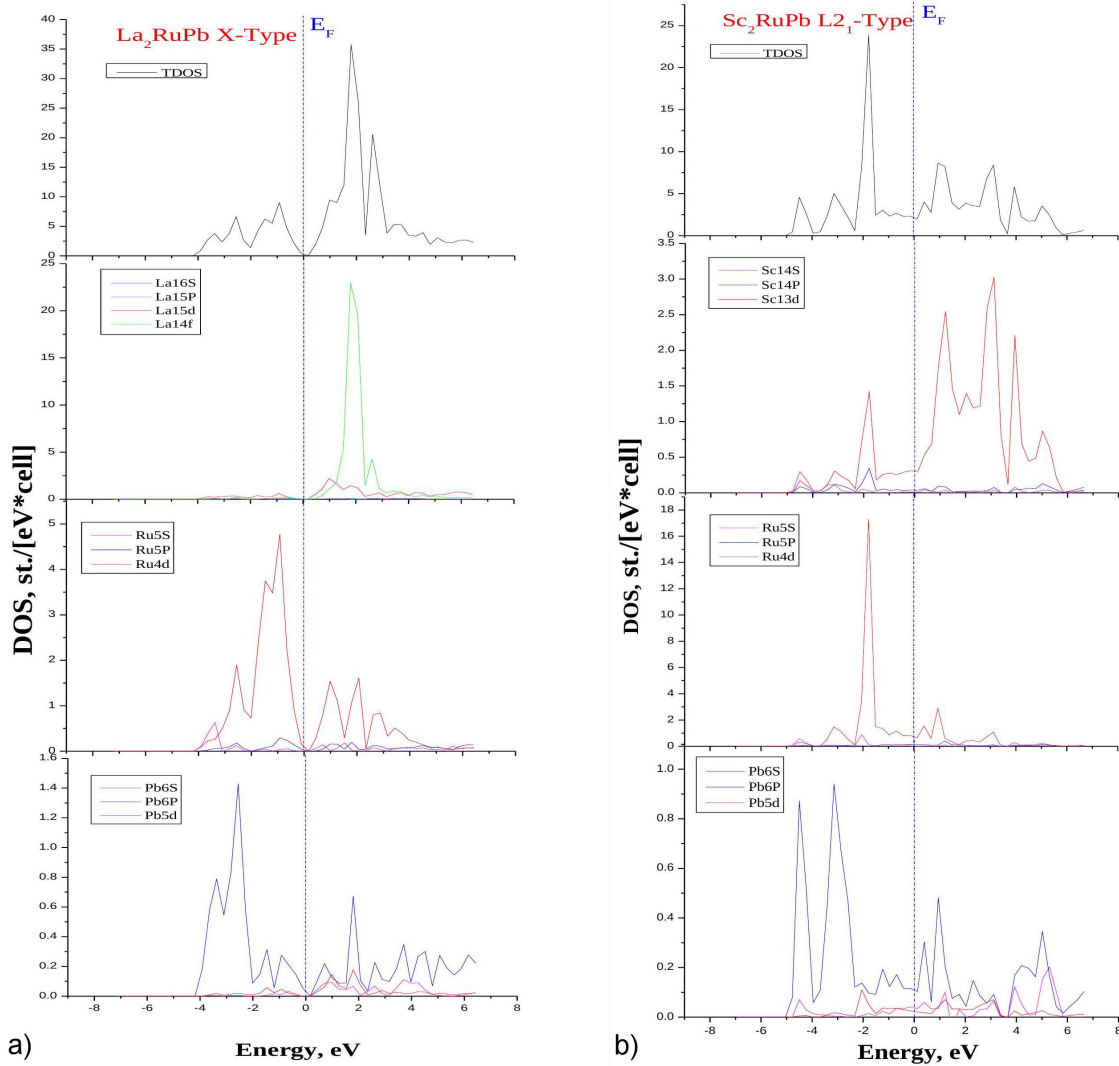


FIGURE 3. The total density of state (TDOS) and the partial density of state (PDOS) for the a)  $\text{La}_2\text{RuPb}$ , b)  $\text{Sc}_2\text{RuPb}$  compounds in the  $\text{Hg}_2\text{CuTi}$ ,  $\text{Cu}_2\text{MnAl}$ -type structure respectively obtained by (LDA) approximation.

atoms in a crystal to be determined. The total state density projections depend on the sphere radius on which the partial state densities are projected and hence only provide qualitative information.

The electronic properties of the  $\text{La}_2\text{RuPb}$ ,  $\text{Sc}_2\text{RuPb}$  compounds in their stable phases  $\text{Hg}_2\text{CuTi}_2\text{Cu}_2\text{MnAl}$  are investigated in the following section by calculating the electronic energy band structure at zero pressure along with the principal symmetry points in the Brillouin Zone, as well as the total density of states (TDOS) and the atomic site-projected I-decomposed partial densities of states (PDOS). For this, we used the (LDA) approximation to inject the theoretical mesh parameter at equilibrium previously determined in the (LmtART) code.

Figures 2a), 2b) and 3a), 3b) show the band structure and plots of the (TDOS) and (PDOS) functions calculated using the LDA of  $\text{La}_2\text{RuPb}$ ,  $\text{Sc}_2\text{RuPb}$  compounds in both crystallographic phases  $\text{Hg}_2\text{CuTi}$ ,  $\text{Cu}_2\text{MnAl}$ . The Fermi level

enables the determination of a material's conduction characteristics. This research aims to figure out how the electronic population varies at Fermi's level  $E_F$ .

Although it is a recognized fact that the self-consistent (DFT) energy-gap calculations at the level of the local density approximation (LDA) exchange-correlation functional are severely underestimated, it is clear from the band structure nature of this compound, as shown in Fig. 2a), that this compound  $\text{La}_2\text{RuPb}$  is a semiconductor with the direct energy bandgap within the following value 0.6044 eV at the  $\Gamma$  point. Moreover, we note that our compound exhibits the Dirac cone-shaped surface energy levels responsible for the topological properties of the (TIs) materials.

It is evident that in Fig. 2b), the non-existence of a gap at the Fermi level for the  $\text{Sc}_2\text{RuPb}$  compound (majority) band's structure has metallic intersections at the Fermi level confirms the assertive metallic behavior and indicates the presence of conducting features. Whereas in Fig. 2a),

the  $\text{La}_2\text{RuPb}$  compound (minority) band's structure exhibits semiconductor behavior, we note an indirect energy bandgap between  $\text{K}_C - \Gamma_V$  points, and it takes the following value 0.398 eV and a direct energy bandgap along  $\Gamma_C - \Gamma_V$  point 0.6044 eV. To the best of our knowledge, there are no theoretical calculations exploring the electronic band structures using the LDA approach for  $\text{La}_2\text{RuPbSc}_2\text{RuPb}$  compounds.

We note that the band profile of the calculated band structure for the  $\text{La}_2\text{RuPb}$  compound is similar to that obtained by Zhang and co-authors [28], with a slight difference due to the absence of spin-orbit in our calculation, which plays a vital role in the band inversion mechanism [34, 35, 68], and in particular, the atoms in (Y-Z) zinc-blende are much heavier than those in (X-X). We should also highlight that, as Zhang *et al.* [28] point out, the band topology in such compounds is very sensitive to variations in lattice constant and uniaxial strain. The  $\text{La}_2\text{RuPb}$  compound combination has a positive energy difference between the  $\Gamma_6$  and  $\Gamma_8$  bands  $\Delta E = E_{\Gamma_6} - E_{\Gamma_8}$ , making it a trivial semiconductor that can be transformed into a nontrivial semiconductor by including spin-orbit coupling (SOC) and controlling the degree of hybridization by firm strain control (constant lattice expansion). We also highlight that our findings are quite similar to Zhang *et al.* [28]. The electronic states' nature (atom and orbital) that create the energy bands may be determined from the spectra (PDOS). The (TDOS) spectrum of the  $\text{La}_2\text{RuPb}$  is separated into two main areas, as shown in Fig. 3a): The first represents the valance band and indicates the mean contribution of the 4d states of the Ru atoms, as well as the low contribution of the 6p states of the Pb atoms included in the combination. The conduction band is represented by the second area, which exhibits a significant contribution from the La atoms' 4f states, with a bit of contribution from the Ru atoms' 4d states.

Concerning the spectrum (TDOS) of the compound  $\text{Sc}_2\text{RuPb}$  shown in Fig. 3b), which is the opposite of the first compound, it can also be divided into two main sections: The first region represents the valance band, which shows the vital contribution of the 4d states of the Ru atoms in addition to the low contribution of the 3d, 6P states of the Sc and Pb atoms, respectively. The second region represents the conduction band; it shows the mean contribution of the 3d states of the (Sc) atoms with a small contribution of the 6P, 4d states of the (Pb, Ru) atoms, respectively.

### 3.4.2. Optical properties

The various methods of light interacting with matter in solid-state physics, including absorption, transmission, reflection, and broadcast, are of significant interest. In addition, the study of solid optical characteristics is a valuable tool in our knowledge of material electronic properties. Understanding the optoelectronic behavior of a material, in particular, requires an understanding of its optical characteristics. The frequency-dependent complex permittivity of light (dielectric function) is the most significant characteristic for describing a

solid's optical properties, and the following relationship provides it [69]:

$$\varepsilon(\omega) = \varepsilon_1(\omega) + i\varepsilon_2(\omega), \quad (15)$$

where  $\varepsilon_1(\omega)$  and  $i\varepsilon_2(\omega)$  are used to represent the real and imaginary parts of the dielectric function, respectively. The imaginary part is given by [70–72]:

$$\varepsilon_2(\omega) = \frac{e^2\hbar}{\Pi\omega^2m^2} \sum_{v,c} \times \int_{BZ} |M_{cv}(k)|^2 \delta[\omega_{cv}(k) - \omega] d^3k. \quad (16)$$

The integral is over the first Brillouin Zone. The momentum dipole elements:  $M_{cv}(k) = \langle u_{ck} | \delta \cdot \nabla | u_{vk} \rangle$ , where  $\delta$  is the potential vector defining the electric field, are matrix elements for direct transitions between valence  $u_{vk}(r)$  and conduction-band  $u_{ck}(r)$  states, and the energy  $\hbar\omega_{cv}(k) = E_{ck} - E_{vk}$  is the corresponding transition energy.

To deduce the real part of the complex dielectric function  $\varepsilon_1(\omega)$  from the imaginary part  $\varepsilon_2(\omega)$ , we use the transformation of Kramers-Kronig [70–72]:

$$\varepsilon_1(\omega) = 1 + \frac{2}{\pi} P \int_0^{\infty} \frac{\omega' \varepsilon_2(\omega')}{\omega'^2 - \omega^2} d\omega', \quad (17)$$

where  $P$  implies the principal value of the Cauchy integral. From the real and imaginary parts of the frequency dependent dielectric function, we can calculate the refractive index  $n(\omega)$  following this relation [73–75]:

$$n(\omega) = \sqrt{\left[ \frac{\varepsilon_1(\omega)}{2} + \frac{\sqrt{\varepsilon_1^2(\omega) + \varepsilon_2^2(\omega)}}{2} \right]}. \quad (18)$$

In this study, we used the optimized structure under equilibrium condition, which is at zero pressure, to compute the refractive index  $n(\omega)$  and the frequency-dependent imaginary and real parts of the dielectric function of the  $\text{La}_2\text{RuPb}$ ,  $\text{Sc}_2\text{RuPb}$  compounds in the ( $\text{Hg}_2\text{CuTi}^2$ ,  $\text{Cu}_2\text{MnAl}$ )-type structures, respectively. Transferring unoccupied bands from occupied bands is a typical process in the electronic energy band structure, especially near the Brillouin Zone's high symmetry points, to explain the optical spectra. The real and imaginary parts of the dielectric function that are frequency dependent are presented in Figs. 4a) and 4b). Photons with energies between [0 and 13.6] eV are used to study the optical response of these materials.

There are multiple significant peaks in the imaginary part of the dielectric function for the two compounds  $\text{La}_2\text{RuPb}$ ,  $\text{Sc}_2\text{RuPb}$  between 1.36-3.538 eV and 0.272-2.449 eV, respectively. These peaks illustrate how the optical transitions from the valance band to the conduction band coincide.

The spectrum also indicates the development of the first optical critical point for the dielectric function at 0.6044 eV

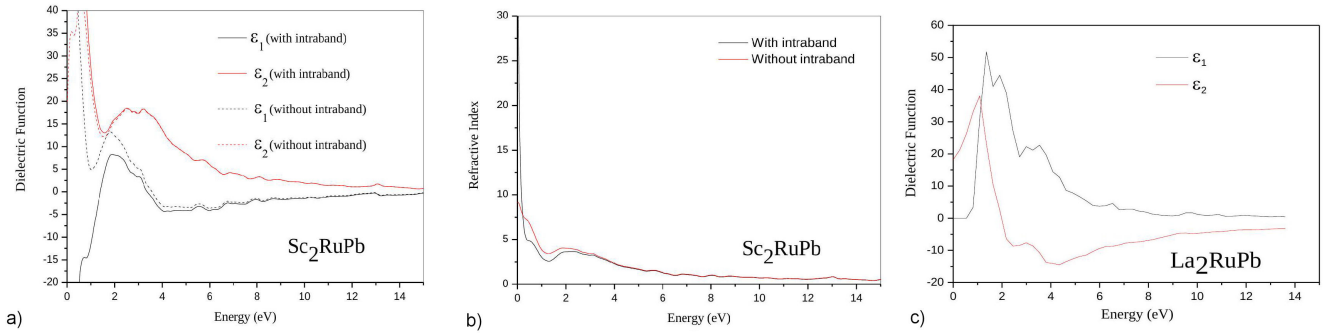


FIGURE 5. The real and imaginary parts of the dielectric function for the a)  $\text{La}_2\text{RuPb}$ , b)  $\text{Sc}_2\text{RuPb}$  compounds in the  $\text{Hg}_2\text{CuTi}$ ,  $\text{Cu}_2\text{MnAl}$ -type structure obtained by (LDA) approximation.

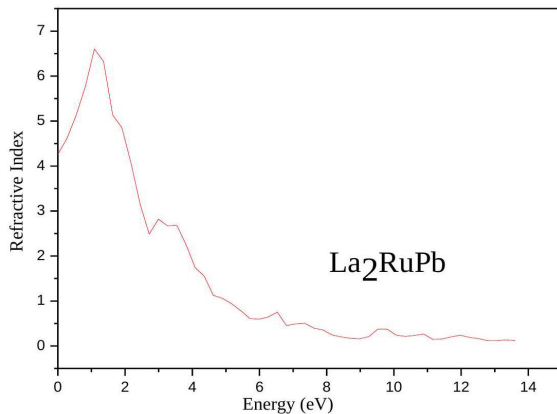


FIGURE 5. The refractive index  $n$  as a function of energy for the a- $\text{La}_2\text{RuPb}$ , b- $\text{Sc}_2\text{RuPb}$  compounds in the  $\text{Hg}_2\text{CuTi}$ ,  $\text{Cu}_2\text{MnAl}$ -type structure respectively obtained by (LDA) approximation.

for the material  $\text{La}_2\text{RuPb}$ , as shown in Fig. 4a). The fundamental absorption edge is placed at the splitting level ( $\Gamma_C - \Gamma_V$ ), representing the direct optical transition threshold between the valence band's maximum and the conduction band's minimum. The spectrum curve overgrows away from this point until it reaches its peak value of 51.763 for 1.36 eV, owing to an unexpected rise in the number of points contributing to the imaginary part. The spectrum of the dielectric function's real part takes the value of 18.1676 at zero 0 eV, reaches a maximum of 38.057 at 1.08 eV, and terminates at zero at 2.1 eV.

For the metallic alloy  $\text{Sc}_2\text{RuPb}$ , we have taken in consideration the strong contribution of the intraband transitions between VBM and CBM [76]. The obtained results show, for low energies, that there is a large difference between the curves of the real part and the imaginary part (with/without intraband), which confirms the strong contribution of the intraband transitions and confirms the strong metallic behavior of this alloy. For the highest energies, we see that the curves are almost similar, and it is obvious, because these transitions are mainly due to the transitions in the bands that overlap (VBM and CBM) close to the fermi level.

As a result, we can see that both compounds  $\text{La}_2\text{RuPb}$ ,  $\text{Sc}_2\text{RuPb}$  have a particular anisotropic property.

We show the calculated dispersion of the refractive index  $n(\omega)$  in the same spectral range in Fig. 5a) and b), which is one of the most critical factors for defining light propagation through the optical medium. Our computed static refractive index  $n(0)$  for the  $\text{La}_2\text{RuPb}$  compound is 4.262, whereas the maximum value of the predicted refractive index was 6.602 at 1.088 eV of photon energy. The static refractive index  $n(0)$  of the second compound  $\text{Sc}_2\text{RuPb}$  was found to be 54.7671 for the curve with intraband transitions and 9.16597 for that without intraband. These latter high values are due to the metallic behavior of this alloy.

#### 4. Conclusion

The main goal of this research was to investigate the structural (phase stability), mechanical, elastic, thermal, electronic, and optical properties of Heusler compounds  $\text{X}_2\text{RuPb}$ , where  $\text{X} = (\text{La}, \text{Sc})$ . The first principle (FP-LMTO) approach was used in the context of the (DFT) implemented in the (LmtART) code to carry out this research. First, the exchange-correlation potential (XC) is calculated using the LDA approximation parameterized by Perdew-Wang.

We started by looking at the structural characteristics of our  $\text{X}_2\text{RuPb}$  compounds, which showed that they are stable in the  $\text{Hg}_2\text{CuTi}$ ,  $\text{Cu}_2\text{MnAl}$  phases. Then, at zero pressure and ambient temperature, we investigated the ground state properties (lattice parameters, bulk modulus  $B$  and its pressure derivative  $B'$ , total energy, and mechanical properties), where all elastic constants were calculated while satisfying the mechanical stability criteria for our compounds. The  $B/G$  ratios for the  $\text{X}_2\text{RuPb}$  compounds indicate ductile materials. In addition, the obtained Debye temperature of  $\text{La}_2\text{RuPb}$  is lower than that of  $\text{Sc}_2\text{RuPb}$ .

We employed the (LDA) approach to study electronic properties, including band structure and state density. With the direct energy bandgap, our compound displays topological insulator characteristics and demonstrates that the gap at  $E_F$  is formed by hybridization between the d-states of the

transition atoms. Furthermore, the structure of the band's findings shows metallic behavior for  $\text{Sc}_2\text{RuPb}$  and semi-conducting behavior for  $\text{La}_2\text{RuPb}$ , with a direct gap in the  $(\Gamma_C - \Gamma_V)$  point and an indirect gap in the  $(K_C - \Gamma_V)$  point. As a result, our materials seem to be semi-metallic.

In addition to their electrical properties, the optical properties of the  $X_2\text{RuPb}$  compounds, including the imaginary parts of the dielectric function and the refractive index  $n(\omega)$ , are also examined in this study.

We discovered satisfactory results for all of the calculated physical attributes in general. The (FP-LMTO) method's ap-

proximation (LDA) seems to be a good fit for the Heusler investigation. Finally, to the best of the authors' knowledge, no data on these compounds can be found in the literature.

## Data availability statement

All relevant data are included in the paper All the data used in the manuscript are produced from the numerical simulations by the authors.

1. F. Heusler, Über magnetische manganlegierungen. *Verhandlungen der Deutschen Physikalischen Gesellschaft* **5** (1903) 219.
2. M. Khirat, *et al.*, First principles calculations of the band ordering conversion in the  $\text{La}_x\text{Sc}_{2-x}\text{RuPb}$  compounds. *Solid State Communications* **276** (2018) 14, <https://doi.org/10.1016/j.ssc.2018.03.018>
3. S. Chadov *et al.*, Tunable multifunctional topological insulators in ternary Heusler compounds. *Nature Mater* **9** (2010) 541, <https://doi.org/10.1038/nmat2770>
4. H. Lin *et al.*, Half-Heusler ternary compounds as new multifunctional experimental platforms for topological quantum phenomena. *Nature Mater* **9** (2010) 546, <https://doi.org/10.1038/nmat2771>
5. R. A. De Groot *et al.*, New class of materials: half-metallic ferromagnets. *Physical review letters* **50** (1983) 2024, <https://doi.org/10.1103/PhysRevLett.50.2024>
6. C. Felser *et al.*, Investigation of a novel material for magnetoelectronics:  $\text{Co}_2\text{Cr}_0.6\text{Fe}_0.4\text{Al}$ . *Journal of Physics: Condensed Matter* **15** (2003) 7019, <https://doi.org/10.1088/0953-8984/15/41/010>
7. D. Kieven, *et al.*, I-II-V half-Heusler compounds for optoelectronics: Ab initio calculations. *Phys. Rev. B* **81** (2010): 075208. <https://doi.org/10.1103/PhysRevB.81.075208>
8. L. Kautzsch, *et al.*, Are AuPd TM (T= Sc, Y and M= Al, Ga, In), Heusler Compounds Superconductors without Inversion Symmetry?. *Materials* **12** (2019) 2580, <https://doi.org/10.3390/ma12162580>
9. Ch. G. F. Blum *et al.*, Exploring the details of the martensite-austenite phase transition of the shape memory Heusler compound  $\text{Mn}_2\text{NiGa}$  by hard x-ray photoelectron spectroscopy, magnetic and transport measurements. *Applied Physics Letters* **98** (2011) 252501, <https://doi.org/10.1063/1.3600663>.
10. B. Dieny, *et al.* Giant magnetoresistive in soft ferromagnetic multilayers. *Phys. Rev. B.* **43** (1991) 1297, <https://doi.org/10.1103/PhysRevB.43.1297>.
11. Heusler, Fr. Magnetismus und Kristallstruktur bei Manganaluminiumkupfer. *Zeitschrift für anorganische und allgemeine Chemie* **161** (1927) 159, <https://doi.org/10.1002/zaac.19271610113>.
12. Y. M. Cho, *et al.* Effects of rapid thermal annealing on the ferromagnetic properties of sputtered  $\text{Zn}_{1-x}(\text{Co} 0.5 \text{ Fe} 0.5) \text{ x O}$  thin films. *Applied Phys. Lett.* **80** (2002) 3358, <https://doi.org/10.1063/1.1478146>
13. A. Bouazza, Sputtering of semiconductors, conductors, and dielectrics for the realization of electronics components thin-films. *Int. J. Thin Film Science and Technology* **11** (2022) 225, <https://doi.org/10.18576/ijtfst/110210>
14. A. Bouazza, Deposition of Thin Films Materials used in Modern Photovoltaic Cells. *Int. J. Thin. Film. Sci. Tec.* **11** (2022) 313, <https://doi.org/10.18576/ijtfst/110308>
15. R. Salah Eddine Chouaib, A. Bouazza, and Y. Belhadji, 3D sputtering simulations of the CZTS, Si and CIGS thin films using Monte-Carlo method. *Monte Carlo Methods and Applications* **27** (2021) 373, <https://doi.org/10.1515/mcma-2021-2094>
16. L. Fu, L. K. Charles, and J. M. Eugene Topological insulators in three dimensions. *Phys. Rev. Lett.* **98** (2007) 106803, <https://doi.org/10.1103/PhysRevLett.98.106803>
17. J. E. Moore, The birth of topological insulators. *Nature* **464** (2010) 194, <https://doi.org/10.1038/nature08916>.
18. Bernevig, B. Andrei, Taylor L. Hughes, and Shou-Cheng Zhang. Quantum spin Hall effect and topological phase transition in  $\text{HgTe}$  quantum wells. *Science* **314** (2006) 1757, <https://doi.org/10.1126/science.1133734>.
19. M. König, *et al.* Quantum spin Hall insulator state in  $\text{HgTe}$  quantum wells. *Science* **318** (2007) 766, <https://doi.org/10.1126/science.1148047>.
20. O. Heusler, Kristallstruktur und Ferromagnetismus der Mangan-Aluminium-Kupferlegierungen. *Annalen der Physik* **411** (1934) 155, <https://doi.org/10.1002/andp.19344110205>.
21. T. Graf, F. Claudia and S.P.P. Stuart, Simple rules for the understanding of Heusler compounds. *Progress in solid state chemistry* **39** (2011) 1, <https://doi.org/10.1016/j.progsolidstchem.2011.02.001>.
22. F. Ahmadian, New Heusler Compounds  $\text{Cr}_2\text{YSb}$  (Y= Fe, Co and Ni): Magnetic and Electronic Properties. *J. superconductivity and novel magnetism* **26** (2013) 1737, <https://doi.org/10.1007/s10948-012-1893-6>.

23. J. Drews, E. Ursula and S. Hans-Uwe, Optische Untersuchungen an farbigen Intermetallischen Phasen. *Journal of the Less Common Metals* **116** (1986) 271, [https://doi.org/10.1016/0022-5088\(86\)90235-3](https://doi.org/10.1016/0022-5088(86)90235-3).
24. N. Tezuka, *et al.* Improved tunnel magnetoresistance of magnetic tunnel junctions with Heusler Co<sub>2</sub>FeAl<sub>0.5</sub>Si<sub>0.5</sub> electrodes fabricated by molecular beam epitaxy. *Applied Phys. Lett.* **94** (2009) 162504, <https://doi.org/10.1063/1.3116717>.
25. X. Dai, *et al.* New quaternary half metallic material CoFeMnSi. *J. Applied Phys.* **105** (2009) 07E901. <https://doi.org/10.1063/1.3062812>.
26. E. Ursula, W. Seelentag, and S. Hans-Uwe, Zur Kenntnis farbiger ternärer und quaternärer Zintl-Phasen/Coloured Ternary and Quaternary Zintl-Phases. *Zeitschrift für Naturforschung B* **35** (1980) 1341, <https://doi.org/10.1515/znb-1980-1103>.
27. W. Feng *et al.* Three-Dimensional Topological Insulators in I-III-VI<sub>2</sub> and II-IV-V<sub>2</sub> Chalcopyrite Semiconductors. *Phys. Rev. Lett.* **106** (2011) 016402, <https://doi.org/10.1103/PhysRevLett.106.016402>.
28. X. M. Zhang *et al.* Prediction of topological insulating behavior in inverse Heusler compounds from first principles. *Computational materials science* **70** (2013) 145, <https://doi.org/10.1016/j.commatsci.2012.12.013>.
29. A. Bouazza, Investigation using Monte-Carlo codes simulations for the impact of temperatures and high pressures on thin films quality. *Rev. Mex. Fis.* **69** (2023) 021501, <https://doi.org/10.31349/RevMexFis.69.021501>
30. A. Bouazza, Simulation of the Deposition of Thin-Film Materials Used in the Manufacturing of Devices with Miniaturized Circuits. *J. Sur. Investigation: X-ray, Synchrotron and Neutron Techniques* **16** (2022) 1221, <https://doi.org/10.1134/S1027451022060283>.
31. A. Bouazza and S. Abderrahmane Understanding the contribution of energy and angular distribution in the morphology of thin films using Monte Carlo simulation. *Monte Carlo Methods and Applications* **24** (2018) 215, <https://doi.org/10.1515/mcma-2018-0019>.
32. A. Bouazza, 3D Visualization of the Effect of Plasma Temperature on Thin-Film Morphology. *Bull. Lebedev Phys. Inst.*, **50** (2023) 7, <https://doi.org/10.1134/S1027451022060283>.
33. Y. Lakred, S. Bahlouli, and M. Elchikh. Electronic and topological properties in heavy-element based Heusler compounds X<sub>2</sub>RuPb (X= Sc, Y, La): first-principle method. *The European Physical Journal B* **94** (2021) 135, <https://doi.org/10.1140/epjb/s10051-021-00141-8>.
34. K. Mun Wong *et al.* First-principles investigation of the size-dependent structural stability and electronic properties of O-vacancies at the ZnO polar and non-polar surfaces. *J. Appl. Phys.* **113** (2013) 014304, <https://doi.org/10.1063/1.4772647>
35. S. Yu. Savrasov, Linear-response theory and lattice dynamics: A muffin-tin-orbital approach. *Phys. Rev. B* **54** (1996) 16470, <https://doi.org/10.1103/PhysRevB.54.16470>.
36. M. Larbi *et al.* First Principle Investigation of Structural, Electronic and Optical Properties of Quaternary B<sub>x</sub>In<sub>y</sub>Ga<sub>1-x-y</sub>N Compounds. *Spin*. **10** World Scientific Publishing Company, 2020. <https://doi.org/10.1142/S2010324720500241>.
37. W. SKohn, Density functional and density matrix method scaling linearly with the number of atoms. *Phys. Rev. Lett.* **76** (1996) 3168, <https://doi.org/10.1103/PhysRevLett.76.3168>.
38. J. P. Perdew, K. Burke, and M. Ernzerhof, Generalized gradient approximation made simple. *Phys. Rev. Lett.* **77** (1996) 3865, <https://doi.org/10.1103/PhysRevLett.77.3865>.
39. S. Y. Savrasov, Program LMTART for electronic structure calculations. *Zeitschrift für Kristallographie-Crystalline Materials* **220** (2005) 555, <https://doi.org/10.1524/zkri.220.5.555.65067>.
40. J. P. Perdew, and W. Yue Pair-distribution function and its coupling-constant average for the spin-polarized electron gas. *Phys. Rev. B* **46** (1992) 12947, <https://doi.org/10.1103/PhysRevB.46.12947>.
41. P. E. Blöchl, Projector augmented-wave method. *Phys. Rev. B* **50** (1994) 17953. <https://doi.org/10.1103/PhysRevB.50.17953>.
42. F. D. Murnaghan, The compressibility of media under extreme pressures. *Proceedings of the National Academy of Sciences* **30** (1944) 244, <https://doi.org/10.1073/pnas.30.9.24>.
43. V. G. Tyuterev, and Nathalie Vast, Murnaghan's equation of state for the electronic ground state energy. *Computational materials science* **38** (2006) 350, <https://doi.org/10.1016/j.commatsci.2005.08.012>.
44. K. Benyelloul, and A. Hafid Elastic constants of austenitic stainless steel: Investigation by the first-principles calculations and the artificial neural network approach. *Comp. Mat. Sci.* **67** (2013) 353, <https://doi.org/10.1016/j.commatsci.2012.09.005>.
45. Y. Ouyang *et al.* First-principles calculations of elastic and thermo-physical properties of Al, Mg and rare earth lanthanide elements. *Physica B: Condensed Matter* **404** (2009) 2299, <https://doi.org/10.1016/j.physb.2009.04.032>.
46. M. J. Mehl *et al.*, Structural properties of ordered high-melting-temperature intermetallic alloys from first-principles total-energy calculations. *Phys. Rev. B.* **41** (1990) 10311, <https://doi.org/10.1103/PhysRevB.41.10311>
47. H. Rached, *et al.* First-principles calculations of structural, elastic and electronic properties of Ni<sub>2</sub>MnZ (Z= Al, Ga and In) Heusler alloys. *Physica Status Solidi (b)* **246** (2009) 1580, <https://doi.org/10.1002/pssb.200844400>
48. F. I. Fedoras, *Theory of Elastic Waves in Crystals.* (1985) 213.
49. M. Born, and K. Huang, *Dynamical theory and experiment I.* Publishers, Berlin (1982).
50. W. J. T. L. Voigt, *Lehrbuch der kristallphysik.* Teubner, Leipzig (1928).

51. A. Reuß, Berechnung der fließgrenze von mischkristallen auf grund der plastizitätsbedingung für einkristalle. *ZAMM-Journal of Applied Mathematics and Mechanics/Zeitschrift für Angewandte Mathematik und Mechanik* **9** (1929) 49, <https://doi.org/10.1002/zamm.19290090104>
52. R. Hill, The elastic behaviour of a crystalline aggregate. *Proceedings of the Physical Society. Section A* **65** (1952) 349, <https://doi.org/10.1088/0370-1298/65/5/307>
53. B. Mayer, *et al.*, Ab-initio calculation of the elastic constants and thermal expansion coefficients of Laves phases. *Intermetallics* **11** (2003) 23, [https://doi.org/10.1016/S0966-9795\(02\)00127-9](https://doi.org/10.1016/S0966-9795(02)00127-9)
54. M. Rajagopalan, Full potential linear augmented plane wave study of the elastic properties of XPt3 (X= V, Cr, Mn, Fe, Co, Ni). *Physica B: Condensed Matter* **405** (2010) 2516, <https://doi.org/10.1016/j.physb.2010.02.060>.
55. J. M. Haines, and G. Bocquillon. *Annu. Rev. Mater. Res* **31** (2001) 1.
56. H. Fu, *et al.* Ab initio calculations of elastic constants and thermodynamic properties of NiAl under high pressures. *Comp. Mat. Sci.* **44** (2008) 774, <https://doi.org/10.1016/j.commatsci.2008.05.026>.
57. I. N. Frantsevich, F. F. Voronov, and S. A. Bokuta. Elastic Constants and Elastic Moduli of Metals and Insulators, ed. IN Frantsevich. (1983).
58. S. F. Pugh, XCII. Relations between the elastic moduli and the plastic properties of polycrystalline pure metals. *The London, Edinburgh, and Dublin Philosophical Magazine and Journal of Science* **45** (1954) 823. <https://doi.org/10.1080/14786440808520496>.
59. Z. E. Biskri, *et al.* Computational study of structural, elastic and electronic properties of lithium disilicate (Li<sub>2</sub>Si<sub>2</sub>O<sub>5</sub>) glass-ceramic. *Journal of the mechanical behavior of biomedical materials* **32** (2014) 345, <https://doi.org/10.1016/j.jmbbm.2013.10.029>.
60. S. Ouardi, *et al.* Electronic and crystallographic structure, hard x-ray photoemission, and mechanical and transport properties of the half-metallic Heusler compound Co<sub>2</sub>MnGe. *Phys. Rev. B.* **84** (2011) 155122. <https://doi.org/10.1103/PhysRevB.84.155122>.
61. Y.-Z. Zhang *et al.* Flexible supercapacitors based on paper substrates: a new paradigm for low-cost energy storage. *Chemical Society Reviews* **44** (2015) 5181, <https://doi.org/10.1039/C5CS00174A>.
62. O. L. Anderson, A simplified method for calculating the Debye temperature from elastic constants. *Journal of Physics and Chemistry of Solids* **24** (1963) 909, [https://doi.org/10.1016/0022-3697\(63\)90067-2](https://doi.org/10.1016/0022-3697(63)90067-2).
63. I. Johnston, Solid state physics simulations. Wiley, 1996.
64. R. E. Newnham, Properties of materials: anisotropy, symmetry, structure. Oxford University Press on Demand, 2005.
65. J. Feng, *et al.* Stability, thermodynamic and mechanical properties of the compounds in the Ag-Sn-O system. *Physica B: Condensed Matter* **404** (2009) 2461, <https://doi.org/10.1016/j.physb.2009.05.004>.
66. E. Schreiber, O. L. Anderson and N. Soga, Elastic Constants, and Their Measurements, McGraw-Hill Companies, Inc., New York, 1973.
67. S. Daoud *et al.* Effect of hydrostatic pressure on the structural, elastic and electronic properties of (B3) boron phosphide. *Pramana* **79** (2012) 95. <https://doi.org/10.1007/s12043-012-0283-8>
68. H. Lin, *et al.* *Nature Mater.* **9** (2010) 546.
69. H. Bouafia *et al.* Insight into elastic anisotropy, mechanical and dynamical stability, electronic properties, bonding and weak interactions analysis of LuAuSn Half-Heusler. *Solid State Sciences* **118** (2021) 106677, <https://doi.org/10.1016/j.solidstatesciences.2021.106677>.
70. C. Ambrosch-Draxl, and J. O. Sofo, Linear optical properties of solids within the full-potential linearized augmented planewave method. *Computer physics communications* **175** (2006) 1, <https://doi.org/10.1016/j.cpc.2006.03.005>.
71. M. Bendjemai *et al.* Insight into the role of weak interactions on optoelectronic properties of LiGaTe<sub>2</sub>-chalcopyrite under pressure effect: DFT-D3, NCI and QTAIM investigations. *Physica B: Condensed Matter* **599** (2020) 412463, <https://doi.org/10.1016/j.physb.2020.412463>.
72. B. Sana *et al.* Study of magnetic and optoelectronic properties of BaMnO<sub>3</sub>-cubic perovskite after the estimation of Hubbard interaction and Hund's exchange parameters: GW and DFT+ U investigations. *Optik* **168** (2018) 196, <https://doi.org/10.1016/j.ijleo.2018.04.064>
73. X-G., Wang *et al.* The hematite ( $\alpha - Fe_2O_3$ )(0001) surface: Evidence for domains of distinct chemistry. *Phys. Rev. Lett.* **81** (1998) 1038. <https://doi.org/10.1103/PhysRevLett.81.1038>
74. A. Delin, *et al.* Optical properties of the group-IVB refractory metal compounds. *Phys. Rev. B.* **54** (1996) 1673. <https://doi.org/10.1103/PhysRevB.54.1673>.
75. Y. U. Peter, and M. Cardona, Fundamentals of semiconductors: physics and materials properties. Springer Science and Business Media, 2010.
76. B. S. Mendoza, and W. Luis Mochán. Ab initio theory of the Drude plasma frequency. *JOSA B* **38** (2021) 1918, <https://doi.org/10.1364/JOSAB.416741>